

Detection of a puzzling dual-superorbital hard X-ray modulation in the X-ray binary GX 301-2

Haoyang Zhang^{1,2}★

¹ Department of Astronomy, Yunnan University, Kunming 650091, China

² Key Laboratory of Astroparticle Physics of Yunnan Province, Yunnan University, Kunming 650091, China

Received XXX / Accepted XXX

ABSTRACT

The superorbital modulations (SMs) observed in wind-fed X-ray binaries remain a puzzling phenomenon in astrophysics. To investigate this behavior observationally, we analyzed the long-term hard X-ray light curve from the *Swift*/BAT 157-Month Hard X-ray Survey in X-ray binary GX 301-2. Using three timing analysis methods—the Lomb-Scargle periodogram, the weighted wavelet Z-transform, and Gaussian processes—we identify a rare dual-SM behavior in this source: the 115-day modulation exceeds the 5σ global significance level, whereas the 65-day signal only marginally reaches the 4σ level. Because the 115-day period is more consistent with the previously reported linear relation between orbital and superorbital periods, we interpret 115 days as the actual superorbital period, while the weaker and less stable 65-day period is its beat modulation with the orbital period. By assessing the applicability of different physical scenarios to our results, we suggest that this dual-SM behavior is most plausibly associated with corotating interaction regions (CIRs) in the stellar wind. This framework can also account for the observed linear orbital–superorbital relation, despite the unclear physical mechanism that sets the apparent ratio between the CIR and orbital periods across sources. Further long-term monitoring of this system, together with continued theoretical development of the CIR scenario, will be essential for clarifying the origin of wind-fed SMs.

Key words. accretion, accretion disks – stars: neutron – X-rays: binaries – pulsars: individual: GX 301-2

1. Introduction

X-ray binaries (XRBs) are the evolutionary products of massive primordial binaries, in which the initially more massive star evolves first and collapses into a compact object (M_X), such as a neutron star or a black hole (Tauris & van den Heuvel 2006). The compact object accretes material lost by its companion, thereby producing bright X-ray emission (see, e.g., Tauris & van den Heuvel 2006; Remillard & McClintock 2006, and references therein). Based on the mass of the companion star (M_2), XRBs are commonly classified into two subclasses: low-mass X-ray binaries (LMXBs; $M_2 \lesssim 1 M_\odot$) and high-mass X-ray binaries (HMXBs; $M_2 \gtrsim 10 M_\odot$). Disk-fed accretion occurs in the majority of LMXBs, whereas in HMXBs a large fraction are wind-fed systems (Bahramian & Degenaar 2023; Fornasini et al. 2023).

In addition to the orbital period of the binary system (typically a few hours to several days), many XRBs exhibit periodic X-ray variability on timescales of a few days to several months, the so-called superorbital modulations (SMs; Sood et al. 2007, and references therein). These signals can sometimes be even stronger than the orbital modulation and may show pronounced temporal evolution (Kotze & Charles 2012). The SMs in black hole XRBs are generally longer than those in neutron star XRBs (see Table 1 of Sood et al. 2007). Corbet et al. (2021) found that wind-fed XRBs follow an approximately linear correlation between the superorbital and orbital periods, which may point to a common physical origin. Further observations will be required to test and refine this framework.

Although the origin of SMs is still not fully understood (especially in wind-fed XRBs), many physical mechanisms have been proposed. Because accretion modes differ among XRBs, the mechanisms responsible for SMs may also differ. In disk-fed systems, SMs are commonly attributed to the precession of a tilted/warped accretion disk driven by radiation-induced warping, magnetic warping, or wind-driven effects (Kotze & Charles 2012). These models can account for both stable and unstable SMs. In wind-fed systems, the situation is more complicated. Moreno et al. (2005) and Koenigsberger et al. (2006) suggested that, in circular orbits, tidally regulated oscillations in the outer layers of the companion star can modulate the mass-loss rate, thereby producing periodic variability. More recently, the interaction between the compact object and large-scale, spiral-shaped structures in the stellar wind—so-called corotating interaction regions (CIRs)—has been proposed to explain long-term and stable SMs (Bozzo et al. 2017; Corbet et al. 2021; Islam et al. 2023; Romano et al. 2025). Chou & Grindlay (2001) proposed that SMs could arise in triple-star systems; however, this scenario typically requires a third body on a distant orbit, making it difficult to explain why most superorbital periods do not exceed three times the orbital period (Corbet & Krimm 2013). In Be/XRBs (neutron-star HMXBs with Be-type companions), SMs may be driven by precession of the Be star’s spin axis (Martin 2023; Chen et al. 2024). In addition, precessing relativistic jets can generate stable SMs, as in the well-known microquasar SS 433 (Kotze & Charles 2012, and references therein).

GX 301-2 (also known as 4U 1223-62) is a classical wind-fed HMXB that hosts an X-ray pulsar with a spin period of ~ 680 s and a mass of $M_X = 1.85 \pm 0.60 M_\odot$, orbiting the supergiant companion Wray 977 (White et al. 1976; Kaper et al. 2006).

★ e-mail: zhanghaoyang@mail.ynu.edu.cn

The system has a rare, highly eccentric orbit ($e \sim 0.47$) with an orbital period of 41.5 days (White & Swank 1984). The companion's mass-loss rate and the pulsar's X-ray luminosity are high, with $\dot{M}_{\text{loss}} \sim 10^{-5} M_{\odot} \text{ yr}^{-1}$ and $L_X \sim 10^{37} \text{ erg s}^{-1}$, respectively (Kaper et al. 2006). The estimated mass and radius of Wray 977 are $M_2 = 43 \pm 10 M_{\odot}$ and $R_2 = 62 R_{\odot}$, respectively (Kaper et al. 2006). Observationally, GX 301-2 shows a regular orbital X-ray flare that consistently occurs ~ 1.4 days before the periastron passage of the X-ray pulsar (Sato et al. 1986; Pravdo & Ghosh 2001). Pravdo et al. (1995) also reported a much weaker and unstable second flare near apastron passage. In addition, the orbit of this binary is decaying on a timescale of $|P_{\text{orb}}/\dot{P}_{\text{orb}}| \sim 0.6 \times 10^5 \text{ yr}$ (Manikantan et al. 2024). Many studies have investigated the X-ray spectral properties during outbursts (e.g., Haberl 1991; Kreykenbohm et al. 2004; Islam & Paul 2014; Liu et al. 2018; Suleimanov et al. 2023; Zalot et al. 2024). Some works suggested that a transient accretion disk may form in GX 301-2 (Koh et al. 1997; Bildsten et al. 1997); however, subsequent observations did not support this interpretation (Nabizadeh et al. 2019).

So far, no SM has been reported in GX 301-2. Given its highly eccentric orbit and distinctive wind-fed accretion properties, further observational investigation of this system is clearly warranted. In this paper, we analyse long-term hard X-ray data from the *Swift*/BAT 157-month survey and report the discovery of a rare dual-SM phenomenon. We suggest that this behavior can be explained within the CIR framework. The rest of this paper is organized as follows. In Sect. 2, we describe the observational data and the timing-analysis techniques used in this work. In Sect. 3, we present the timing results and discuss the possible physical origin of the SM. Finally, in Sect. 4, we briefly summarize our main findings.

2. Observations and Data Analysis

Recently, Lien et al. (2025) released a high-quality, long-term hard X-ray monitoring dataset with a uniform observing cadence, enabling an efficient search for SMs on timescales ranging from several days to years. For the timing analysis, we employ three methods—the Lomb-Scargle periodogram (LSP), the weighted wavelet Z-transform (WWZ), and Gaussian processes (GP) to identify candidate periodic signals. The first two are classic frequency-domain techniques, whereas GP provides a time-domain approach based on model fitting and has gained broad popularity in recent years (Aigrain & Foreman-Mackey 2023).

2.1. *Swift*/BAT 157-Month Hard X-ray Survey

Mounted aboard the *Swift* observatory is the Burst Alert Telescope (BAT), designed primarily for the detection and monitoring of γ -ray bursts (Barthelmy et al. 2005). The *Swift*/BAT all-sky survey spanning 157 months (2004–2017) has identified 1888 reliable sources (Lien et al. 2025). Most of these detections are active galactic nuclei (AGNs), while XRBs constitute approximately 13% of the catalog. The BAT light curves in eight energy bands (14–20, 20–24, 24–35, 35–50, 50–75, 75–100, 100–150, and 150–195 keV) were pre-processed by Lien et al. (2025) using the standard BAT reduction pipeline. For each source, a detection threshold of 4.8σ was adopted to ensure a high signal-to-noise ratio in the light curves. In Lien et al. (2025), the eight-band fluxes were further combined to generate a Crab-calibrated 14–195 keV light curve, using the Crab spectrum as the reference. The resulting light curves span ~ 157 months and have an effective cadence of about one month. All BAT 14–195

keV Crab-calibrated light curves are publicly available on the official *Swift* website¹.

For GX 301-2 (SWIFT J1226.6-6244), in the 14–195 keV band, the light curve has a total signal-to-noise ratio of 2330.17 and a mean flux of $2842.04 \pm 1.83 \times 10^{-12} \text{ erg s}^{-1} \text{ cm}^{-2}$. Before performing the timing analysis, we discarded data points with exposure times shorter than one day, a filtering step that has been shown to efficiently remove measurements with excessively large uncertainties (Mundo & Mushotzky 2023).

2.2. Timing Analysis Methods

LSP is a frequency-domain analysis tool analogous to the Fourier transform, developed by Lomb (1976) and Scargle (1982). Technically, the LSP identifies periodic signals by fitting sinusoidal functions to the data at a range of trial frequencies, which makes it particularly effective for analyzing irregularly sampled time series. For a flux time series $F(t_i)$ (where $i = 1, 2, 3, \dots, N$), the LSP periodogram is given by:

$$P_{\text{LS}}(f) = \frac{1}{2} \left\{ \left[\sum_i F(t_i) \cos \omega(t_i - \tau) \right]^2 / \sum_i \cos^2 \omega(t_i - \tau) \right. \\ \left. + \left[\sum_i F(t_i) \sin \omega(t_i - \tau) \right]^2 / \sum_i \sin^2 \omega(t_i - \tau) \right\}, \quad (1)$$

where $\omega = 2\pi f$ is the angular frequency and τ is specified for each f to ensure time-shift invariance:

$$\tau = \frac{1}{2\omega} \tan^{-1} \left[\sum_i \sin(2\omega t_i) / \sum_i \cos(2\omega t_i) \right]. \quad (2)$$

In principle, the effective frequency range spans from $1/T_{\text{total}}$ to $1/(2\Delta t)$, where T_{total} is the light-curve baseline and $\Delta t = 30$ days is the sampling interval. Although we excluded data points with exposure times shorter than one day, the maximum effective frequency, $1/(2\Delta t)$, should remain unchanged (VanderPlas 2018). Because XRB light curves are typically dominated by white/red noise, apparent periodicities supported by only 2–3 cycles are often non-physical (Vaughan et al. 2016). We therefore set the upper and lower bounds of the searched frequency range to $1/60$ and 10^{-3} days⁻¹, respectively.

To estimate the significance of candidate peaks, we adopted a simulated-background-noise approach (Timmer & König 1995). We used the code developed by Emmanoulopoulos et al. (2013) to fit the power spectral density (PSD) and generated 3×10^7 artificial light curves. Over the searched frequency range, the PSD of this source is consistent with a typical white-noise shape. Since we have no prior information on the peak location, we account for the “look-elsewhere” effect (i.e., global significance; Gross & Vitells 2010). Following Covino et al. (2019), we used the statistic $T_R = \max R_j$ to evaluate the global significance of any peak in the PSD, with sensitivity up to the 5σ level, where $R = 2P/S$, P is the simulated or observed PSD, and S is the best-fit PSD model.

The second timing method used in this work is the WWZ (Foster 1996). Unlike the LSP, it can track the temporal evolution of frequency components by combining a wavelet transform with a Z-transform. Following Foster (1996), the WWZ two-dimensional map is given by:

$$W[\omega, \tau; F(t)] = \omega^{1/2} \int F(t) f^*[\omega(t - \tau)] dt \quad (3)$$

¹ <https://swift.gsfc.nasa.gov/results/bs157mon/>

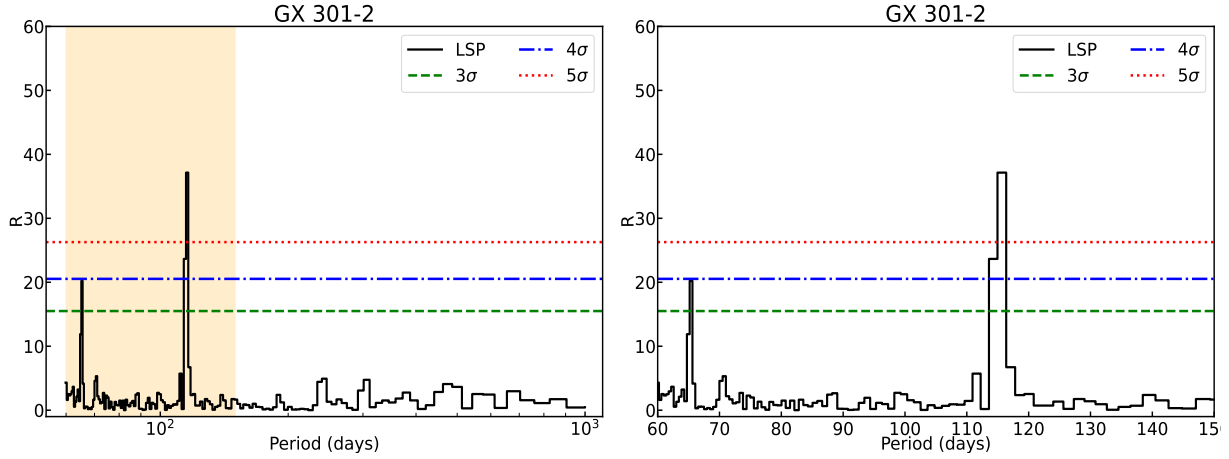


Fig. 1. LSP of the long-term *Swift*/BAT 14–195 keV light curve of GX 301-2. The periodograms are shown in terms of the R statistic as a function of trial period. The left panel shows the full period range, while the right panel zooms into the yellow-shaded interval highlighted in the left panel. The dashed horizontal lines mark the global significance thresholds at 3σ (green), 4σ (blue), and 5σ (red). Two candidate superorbital modulations are detected at ~ 65 days and ~ 115 days, with the ~ 115 days peak exceeding the 5σ level.

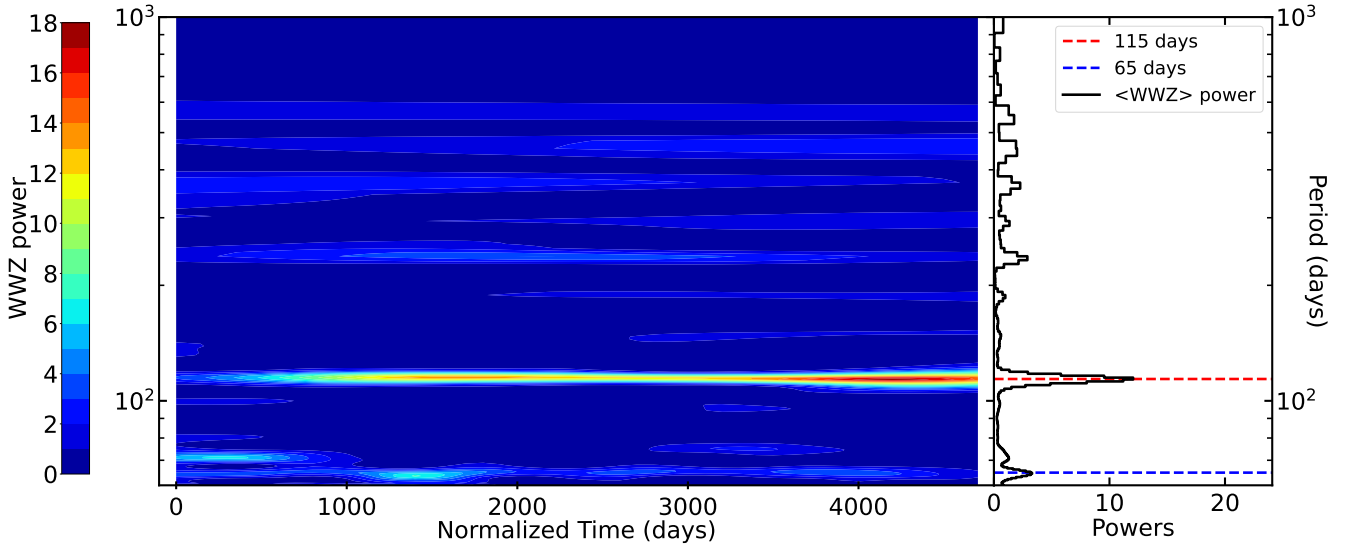


Fig. 2. WWZ analysis of the long-term *Swift*/BAT 14–195 keV light curve of GX 301-2. The left panel shows the WWZ power as a function of normalized time and trial period, highlighting the temporal evolution of periodic components. The right panel displays the time-averaged WWZ power spectrum as a function of period. The dashed horizontal lines mark the 115-day (red) and 65-day (blue) candidate superorbital periods; the ~ 115 -day component remains prominent across most of the baseline, whereas the ~ 65 -day signal is comparatively weaker.

where t is the time shifts, ω is the angular frequency and $f^*[\omega(t-\tau)]$ can be defined as $\exp[-i\omega(t-\tau) - c\omega^2(t-\tau)^2]$, which is the complex conjugate of the Morlet kernel. The sensitivity of the 2D time-frequency power map is determined by the window size factor c .

Over the past decade, driven by advances in time-domain astronomy, Gaussian processes (GPs) have been widely adopted and have become an important tool in astronomical data analysis (Aigrain & Foreman-Mackey 2023, for a review). In particular, GPs can parameterize the stochastic processes underlying a time series by specifying a mean function and a covariance function, without requiring an explicit physical or mathematical form for the generative process (Hübner et al. 2022b). Moreover, the GP framework naturally lends itself to Bayesian inference, allowing the light curve to be fit directly using Markov Chain Monte Carlo (MCMC). In GP, the log-likelihood for a time series $y = f(t) + \sigma$,

where σ denotes the measurement error, can be written as:

$$\ln \mathcal{L}(\theta, \alpha) = -\frac{1}{2} \mathbf{r}_\theta^T K_\alpha^{-1} \mathbf{r}_\theta - \frac{1}{2} \ln \det K_\alpha - \frac{N}{2} \ln(2\pi). \quad (4)$$

where $\mathbf{r}_\theta = \mathbf{y} - \mu_\theta(t)$, $\mu_\theta(t)$ is the mean function, $[K_\alpha]_{nm} = k_\alpha(t_n, t_m) + \sigma_n^2 \delta_{nm}$, $k_\alpha(t_n, t_m)$ is the covariance function, δ_{nm} is the Kronecker delta symbol, and N is number of data points of the time series. θ and α denote the hyperparameters of the mean function and the covariance function, respectively.

For the detection of periodic signals, GPs also show great potential (e.g., Covino et al. 2020; Zhu & Thrane 2020; Yang et al. 2021; Hübner et al. 2022b; Zhang et al. 2023; Sharma et al. 2024). Here, we adopt a widely used GP modeling package, *celerite*, developed by Foreman-Mackey et al. (2017). In *celerite*, the covariance function is expressed as a mixture of exponentials, $k_\alpha(t_n, t_m) = \sum_{j=1}^J a_j \exp(-c_j \tau_{nm})$, where $\tau_{nm} \equiv |t_n - t_m|$ and J is the number of mixture components.

To model periodic behavior, we use the stochastically driven damped simple-harmonic oscillator (SHO) kernel (covariance function). The differential equation for this system is:

$$\left[\frac{d^2}{dt^2} + \frac{\omega_0}{Q} \frac{d}{dt} + \omega_0^2 \right] y(t) = \epsilon(t), \quad (5)$$

where ω_0 is the frequency of the undamped oscillator, Q is the quality factor, and $\epsilon(t)$ is assumed to be white noise. Then, the PSD of this model can be written as:

$$S(\omega) = \sqrt{\frac{2}{\pi}} \frac{S_0 \omega_0^4}{(\omega^2 - \omega_0^2)^2 + \omega_0^2 \omega^2 / Q^2}, \quad (6)$$

where S_0 is proportional to the power at $\omega = \omega_0$ (corresponding to the angular frequency of a periodic signal) and $S(\omega_0) = \sqrt{2/\pi} S_0 Q^2$. If the model captures a periodic signal, then Q must be greater than 0.5 (Foreman-Mackey et al. 2017). Generally, the superposition or product of kernel functions is regarded as an effective way to describe more complex periodic behaviors (Covino et al. 2020; Yang et al. 2021), such as multi-periodic behaviors. If the model captures a periodic signal, then Q must be greater than 0.5 (Foreman-Mackey et al. 2017). In general, superpositions or products of kernel functions provide an effective way to model more complex periodic behavior (Covino et al. 2020; Yang et al. 2021), such as multi-periodic variability.

To reduce potential instabilities in the maximum-likelihood optimization with L-BFGS-B, we run the fitting procedure 100 times using different initial parameter values. The maximum-likelihood solution is then used to initialize the MCMC sampling. Using `emcee`, developed by Foreman-Mackey et al. (2013), we perform 15000×32 iterations with 32 parallel chains, discarding the first 5000 iterations as burn-in and retaining the remaining 10000 iterations from each chain for posterior sampling.

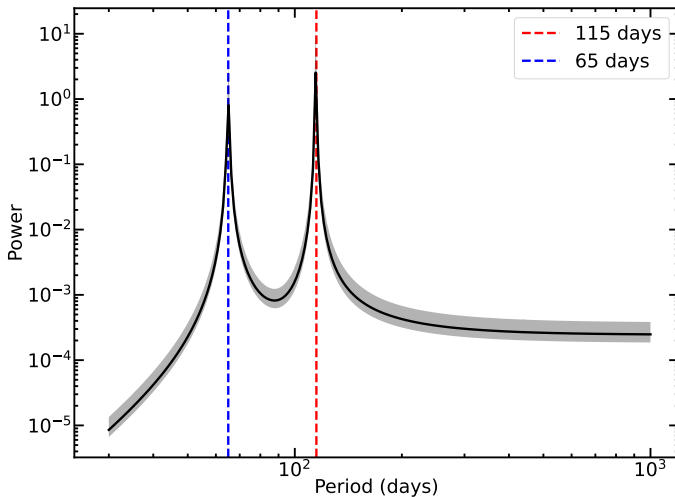


Fig. 3. PSD of the best-fit GP model (SHO + SHO) for the long-term Swift/BAT 14–195 keV light curve of GX 301-2. The black curve shows the model PSD, and the shaded region indicates the uncertainty derived from the posterior distribution. Two clear periodic components are present, with peaks at ~ 65 days and ~ 115 days, marked by the blue and red dashed lines, respectively.

If the model captures the underlying behavior of the time series, the standardized residuals (SRs) should be consistent with white noise, i.e., $r_{\text{std}} \sim \mathcal{N}(0, 1)$. We use the Kolmogorov-Smirnov (K-S) test to quantify this criterion: a distribution consistent with white noise should have a K-S P -value greater than

0.05. In addition, the autocorrelation functions (ACFs) of the SRs and of the squared SRs should lie within the 95% confidence interval expected for white noise (Kelly et al. 2014).

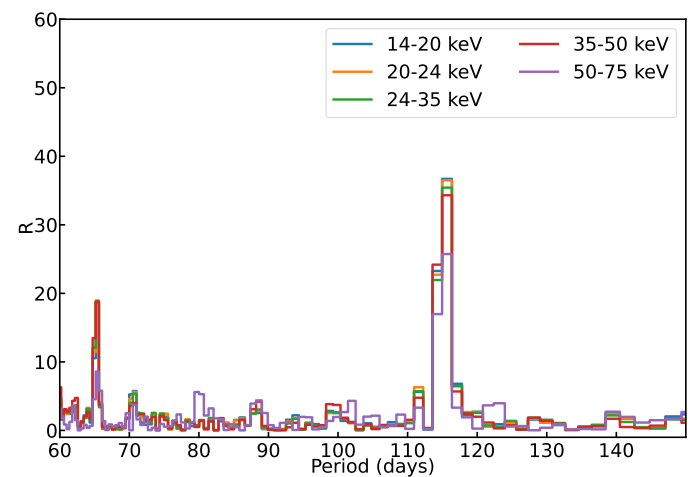


Fig. 4. Energy-resolved LSPs of GX 301-2 in selected Swift/BAT bands. The dual-SM signatures at ~ 115 days and ~ 65 days progressively weaken with increasing energy and become undetectable above 75 keV.

3. Results and Discussion

3.1. Timing Analysis Results

The LSP results are shown in Fig. 1. The periodograms are shown in terms of the R statistic as a function of trial period. In the left panel, we identify two prominent peaks at 65 and 115 days. The longer-period peak exceeds the 5σ global significance level, whereas the shorter-period peak only marginally reaches the 4σ level. The right panel shows a zoomed-in view of the region highlighted by the yellow shaded band in the left panel.

The WWZ results, which illustrate the temporal evolution of these two signals, are presented in Fig. 2. Because the 65-day signal remains persistently weak over the full observational baseline, its mean WWZ power is reduced, as shown in the right panel. In contrast, the 115-day signal is strong over nearly the entire duration. These trends further support the LSP results.

To validate the LSP detections, we fitted the light curve with a combined GP model (SHO + SHO). This model consists of two periodic kernels and is capable of capturing two periodic components. The modeling results are shown in Fig. A.1 in Appendix A: the top panel presents the best-fit (SHO + SHO) model, and the bottom panel shows the residual diagnostics. The K-S test yields $P = 0.28$, indicating that the standardized residuals (SRs) are consistent with white noise. The ACFs of the SRs and of the squared SRs also lie almost entirely within the 95% confidence interval expected for white noise. The PSD of the fitted model can be derived directly from Eq. 6, and we show it in Fig. 3. The peak locations agree with those found by the LSP. We also present the posterior distributions of the model parameters in Fig. A.2 in Appendix A.

All three timing analysis methods have identified that this source contains a rare dual SM signal. It is worth noting that many periodic signals, which were reported to have high significance, were rejected in the GP study. Specifically, Yang et al. (2021) and Zhang et al. (2023) used the GP method to verify sources in AGN that had previously been reported to exhibit periodic signals. The results showed that only a small number of

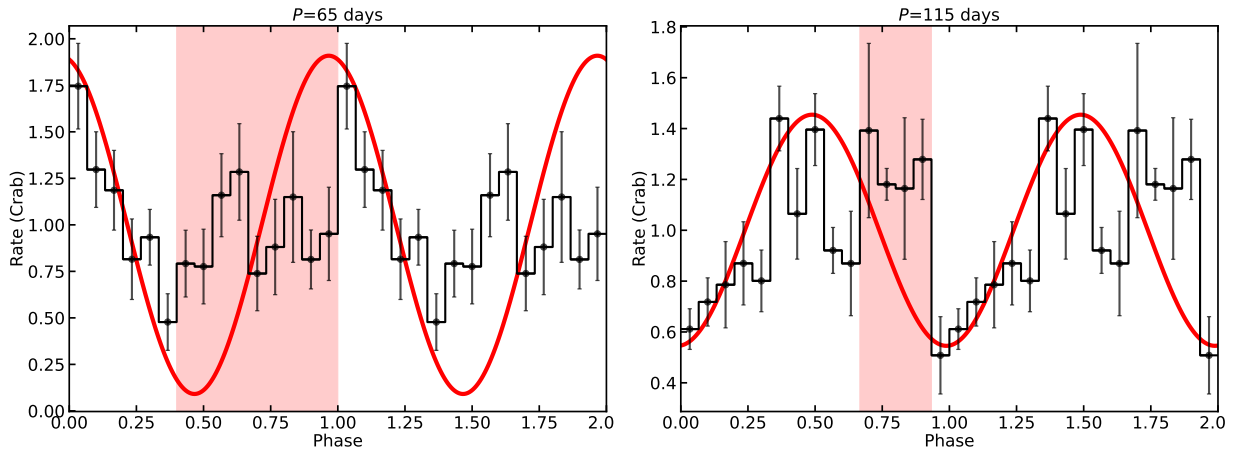


Fig. 5. Phase-folded *Swift/BAT* 14–195 keV light curves of GX 301-2 folded at $P = 65$ days (left) and $P = 115$ days (right). The black points with error bars show the folded data, while the red curves indicate the assumed sinusoidal trends. The red shaded regions highlight additional phase-localized excesses relative to a pure sinusoid, demonstrating departures from a simple sinusoidal modulation in both folded profiles.

sources with extremely high significance were confirmed by the GP method, such as RE J1034+396, which was reported in the literature (Jin et al. 2020) to exceed the 9σ global significance level. The exact cause of this discrepancy is currently unknown. There are three possible reasons: (i) Most studies rely on the local significance method to estimate the peaks from suspected periodic signals. However, this approach is statistically unreliable unless there are additional observations that provide prior information about the candidate periodic signal. (ii) Traditional frequency-domain methods are susceptible to the effects of data baseline variations and observation cadence, leading to red-noise leakage and aliasing in the PSD. (iii) When generating simulated light curves, it is crucial to assess whether the model used for fitting the observed PSD adequately captures the true background PSD. Several studies have reported that AGN PSDs may contain high-frequency features that are more complex than those represented by power-law or bending power-law models (e.g., Stone et al. 2022; Yu et al. 2022; Xu et al. 2025; Yu et al. 2025). (iii) The nonstationarity bias of periodograms (Hübner et al. 2022a). A more detailed discussion of these issues is beyond the scope of this work. Nevertheless, by using the GP method to validate the LSP results, we are confident that our findings are robust.

In addition to the total-band (14–195 keV) light curve, Lien et al. (2025) also provided eight energy-resolved light curves in units of counts s^{-1} . Using the same procedure as for the total band, we computed the corresponding PSDs, which are shown in Fig. 4. The periodic features progressively weaken as the energy increases, becoming indistinguishable above 75 keV. To prevent severe visual overlap, we have omitted energy-resolved PSDs that do not exhibit significant periodic peaks.

This apparent energy dependence is likely due to data quality rather than intrinsic source behavior. Above 35 keV, the light-curve uncertainties increase significantly due to the low count rates, which strongly suppress the detectability and significance of periodic signals. To quantify this effect, we calculated the average signal-to-noise ratio for each band, defined as $\text{SNR}_{\text{average}} = \langle \text{Rate} \rangle / \langle \sigma \rangle$. The SNRs in the 14–20, 20–24, and 24–35 keV bands are approximately 190, 174, and 147, respectively. However, the SNR drops to 36 in the 35–50 keV band and to 5 in the 50–75 keV band, with the SNR falling below unity at higher energies. We therefore interpret the disappearance of the periodic features above 75 keV as most likely non-physical. We

speculate that the modulation may persist across the hard X-ray band, but becomes undetectable in the highest-energy channels due to the current statistical limitations.

To study the phase shape of the dual SM, we used the `efold` tool to fold the light curves using two periods: 65 days and 115 days, respectively. Assuming that the actual SM is sinusoidal, both phase-folded light curves exhibit an additional component that disrupts the sinusoidal shape, as shown by the red shading in Fig. 5. This suggests that the two SMs are strongly coupled and mutually influential. We also found that either of the two SMs can be precisely expressed as the beat frequency between the orbital period and the other SM, i.e.,

$$f_{\text{sup1}} = f_{\text{orb}} - f_{\text{sup2}}, \quad (7)$$

where $f_{\text{orb}} = 1/41.5 \text{ days}^{-1}$ for GX 301-2 (White & Swank 1984).

Over the past decade, Corbet & Krimm (2013) and Corbet et al. (2021) reported a correlation between the orbital period and the superorbital period in wind-fed XRBs. However, at the time of writing, only seven binary systems were used to establish this relation (see Table 2 of Corbet et al. 2021), and its physical origin remains poorly understood. Here, we incorporate the SMs reported in this work into this correlation. In Fig. 6, the black points show the previously reported SMs compiled from Corbet et al. (2021), while the red and purple points correspond to the two SM candidates identified in this work. We perform linear fits for three cases: the literature sample alone (S_A), the literature sample plus the 65-day signal (S_B), and the literature sample plus the 115-day signal (S_C). All three fits indicate a strong correlation, with Pearson coefficients of $r_{\text{pearson}} = 0.994$, 0.992, and 0.999 for S_A , S_B , and S_C , respectively. Notably, the slope obtained for S_C is closer to that of S_A , and adding the 115-day point further strengthens the correlation (from 0.994 to 0.999), whereas adding the 65-day point slightly weakens it. Combined with Eq. 7, these results further suggest that the 65-day signal is more likely the beat frequency between the 115-day modulation and the orbital period. More generally, because astrophysical systems cannot be described by simple geometric configurations, the mechanisms driving X-ray variability are inherently complex; thus, even modest perturbations to periodic components can affect the strength and coherence of the beat modulation. Our WWZ results support this interpretation.

Consequently, our results not only provide further support for this important relationship, but also suggest that $P_{\text{SM}}=115$ days is the actual superorbital period, whereas $P_{\text{SM}}=65$ days is merely the beat frequency with the orbital period.

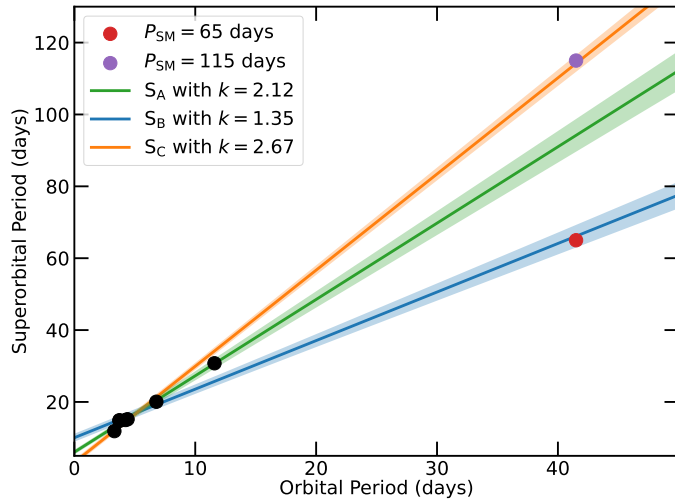


Fig. 6. Correlation between orbital period and superorbital period for wind-fed XRBs. Black points show previously reported sources compiled from the literature, while the red and purple points mark the two SM candidates in GX 301-2 ($P_{\text{SM}} = 65$ and 115 days). The solid lines show linear fits for three cases: S_A (green), S_B (blue), and S_C (orange). Shaded bands indicate the corresponding 1σ uncertainties.

3.2. Possible Physical Mechanisms

We begin by considering the most classic physical scenario: the existence of a transient accretion disk around the X-ray pulsar. The precessing warped disk can drive the SM in a circular orbit (Ogilvie & Dubus 2001). However, for GX 301-2, Nabizadeh et al. (2019) proposed that X-rays are primarily driven by wind accretion. Furthermore, the periodic signals we detected were stable and persistent, particularly the 115-day SM. Ogilvie & Dubus (2001) demonstrated that the stability of the warped disk precession model depends on the mass ratio $q = M_2/M_X$ and the semimajor axis a in a circular orbit. The semimajor axis of GX 301-2 is $177R_\odot$ (Manikantan et al. 2024), allowing us to calculate that GX 301-2 is located in the chaotic region shown in Figure 7 of Ogilvie & Dubus (2001). Additionally, GX 301-2 is a binary star system with an eccentricity of 0.47 (White & Swank 1984). Therefore, the SM we detected is unlikely to be driven by the transient accretion disk.

Next, we discuss the changes in the accretion rate induced by the oscillations of the companion star, which drives the SM (Moreno et al. 2005; Koenigsberger et al. 2006). However, similar to the precession disk model, this physical scenario requires a circular orbit (Farrell et al. 2008). Therefore, it is unlikely that this mechanism drives the SM in GX 301-2.

For non-circular orbit XRBs, such as stellar triple systems, both the precession of the companion star and the CIR model can serve as the origin of the SM. In a triple-star system, the third outer body can induce quasi-periodic signals with a period given by $P_{\text{SM}} = P_2^2/P_1$ (Zdziarski et al. 2007), where $P_1 = 41.5$ days is the inner orbital period in our source and P_2 is the unknown outer orbital period. Assuming that the 115-day SM is driven by this physical mechanism, we calculate that the outer orbital period of the triple-star system is 69.08 days. The ratio of the

semimajor axes of the outer and inner orbits can be derived from Kepler's laws:

$$a_2/a_1 = (P_2/P_1)^{2/3} = 1.40 \quad (8)$$

Such close values for the inner and outer semimajor axes imply that the system may be unstable (Coley et al. 2019). However, previous studies on the orbital periods and SM detected in this work have not identified this characteristic.

In the precessing companion star model, a decretion disk locked to the equator of companion can produce X-ray periodic signals via precession about rotational axis of the companion star (Martin 2023). Unlike the warped-disk scenario, this mechanism can operate in systems with relatively large eccentricities, such as GX 301-2. The precession angular frequency of the companion's spin axis can be written as

$$\omega = \frac{3}{2q} k \Omega_2 \left(\frac{R_2}{a(1-e^2)^{1/2}} \right)^3 \cos i \quad (9)$$

where $k \approx 0.5$ (Martin 2023), q is the mass ratio, i is the angle between spin axis of the companion star and the binary orbit, and $\Omega_2 = v_e/R_2$ is the spin angular frequency of the companion star. For GX 301-2, $v_e = 61 \text{ km s}^{-1}$ (Manikantan et al. 2024). Taking $\cos i = 1$, we obtain a minimum spin-axis precession period of ~ 70 years. Such a long period could, in principle, yield a detectable SM via beating with the orbital period (Zhang 2024). However, because $\omega \ll \Omega_{\text{orb}}$ the resulting beat frequency would be extremely close to the orbital frequency, which is inconsistent with the observed 65 and 115-day signals.

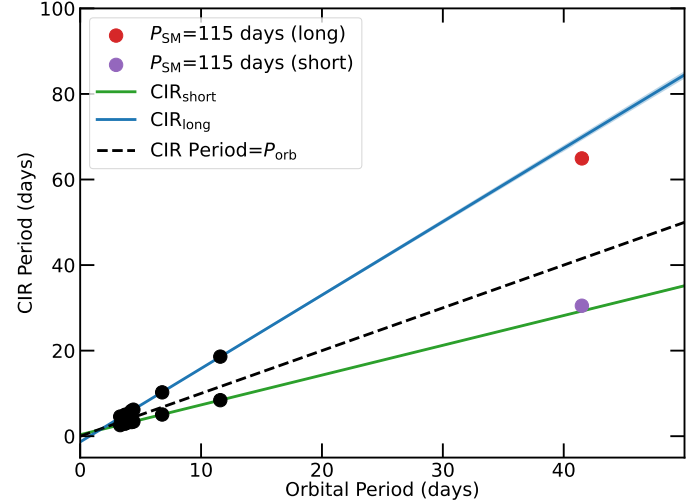


Fig. 7. Comparison of GX 301-2 with the relation between the CIR rotation period and the orbital period proposed by Corbet et al. (2021). Black points show the source sample used to establish the correlation. The red and purple points indicate the CIR periods inferred from our two SM candidates under the CIR beat-frequency framework. The solid green and blue lines show the two branches of the proposed relation ($\text{CIR}_{\text{short}}$ and CIR_{long}), while the black dashed line marks $P_{\text{CIR}} = P_{\text{orb}}$ for reference.

The final physical scenario that may induce the SM is the CIR model. In this picture, one or more large-scale CIRs rotate non-synchronously with respect to the binary orbit, thereby modulating the wind accretion onto the neutron star and driving X-ray variability in wind-fed pulsars, particularly in low-eccentricity systems ($e \lesssim 0.2$) (Bozzo et al. 2017). The SM then naturally arises as a beat period between the orbital motion and

the CIR pattern rotation. In principle, two regimes are possible: the CIR pattern period P_{CIR} may be longer than the orbital period, or shorter than it. [Corbet et al. \(2021\)](#) argued that the CIR model can account for most wind-fed SMs and presented a unified relation followed by multiple sources within this framework (see the blue and green lines in Fig. 7).

Our results favor the regime in which the CIR pattern rotates faster than the orbit. Under this assumption, the implied CIR period is $P_{\text{CIR}} = 30.5$ days (purple points in Fig. 7), which can be naturally accommodated by the unified relation. For GX 301-2, the rotation period of the star can be roughly estimated as $P_{\text{spin}} \approx 2\pi R_2/v_e \approx 51$ days. The fact that $P_{\text{CIR}} < P_{\text{spin}}$ suggests that the CIR may be associated with spots located at higher latitudes, whose rotation period can exceed the spin of the star due to differential rotation ([Ramiaramantsoa et al. 2018](#); [Corbet et al. 2021](#)). If the SM in GX 301-2 is indeed produced by such CIRs, the CIR framework provides a straightforward explanation for the observed correlation between the orbital and superorbital periods (Fig. 6). Nevertheless, it remains unclear what physical mechanism enforces an approximately fixed ratio between P_{CIR} and the orbital period across different sources. Moreover, the role of high orbital eccentricity, such as $e = 0.47$ in GX 301-2, may be important for the CIR interaction geometry and deserves further investigation.

4. Conclusion

In summary, we employed three timing analysis methods to analyze the long-term hard X-ray light curve of GX 301-2 and detected a rare dual SM signal. The longer SM of 115 days shows a stable trend over more than 10 years in the WWZ two-dimensional map, whereas the shorter SM of 115 days is weaker and exhibits more pronounced temporal fluctuations. Combined with the established correlation between the orbital and superorbital periods, we suggest that 115 days represents the actual superorbital signal, while 65 days corresponds to its beat modulation with the orbital period.

By comparing several physical mechanisms proposed in the literature, we argue that the CIR model is a plausible explanation for the SM detected in this work. Moreover, the CIR framework may also account for the puzzling correlation between the orbital and superorbital periods. However, the physical origin of the apparently fixed ratio between the P_{CIR} and the orbital period across different sources remains unclear. Further long-term observations of this source, together with continued theoretical and observational studies of the CIR model, may be essential for resolving this issue.

Acknowledgements. We especially thank the Lien, A. group for providing the *Swift*/BAT 157-Month Hard X-ray Survey data.

References

Aigrain, S. & Foreman-Mackey, D. 2023, *ARA&A*, 61, 329

Bahramian, A. & Degenaar, N. 2023, in *Handbook of X-ray and Gamma-ray Astrophysics*, 120

Barthelmy, S. D., Barbier, L. M., Cummings, J. R., et al. 2005, *Space Sci. Rev.*, 120, 143

Bildsten, L., Chakrabarty, D., Chiu, J., et al. 1997, *ApJS*, 113, 367

Bozzo, E., Oskinova, L., Lobel, A., & Hamann, W.-R. 2017, *A&A*, 606, L10

Chen, A. M., Takata, J., & Yu, Y. W. 2024, *ApJ*, 973, 162

Chou, Y. & Grindlay, J. E. 2001, *ApJ*, 563, 934

Coley, J. B., Corbet, R. H. D., Fürst, F., et al. 2019, *ApJ*, 879, 34

Corbet, R. H. D., Coley, J. B., Krimm, H. A., Pottschmidt, K., & Roche, P. 2021, *ApJ*, 906, 13

Corbet, R. H. D. & Krimm, H. A. 2013, *ApJ*, 778, 45

Covino, S., Landoni, M., Sandrinelli, A., & Treves, A. 2020, *ApJ*, 895, 122

Covino, S., Sandrinelli, A., & Treves, A. 2019, *MNRAS*, 482, 1270

Emmanoulopoulos, D., McHardy, I. M., & Papadakis, I. E. 2013, *MNRAS*, 433, 907

Farrell, S. A., Sood, R. K., O'Neill, P. M., & Dieters, S. 2008, *MNRAS*, 389, 608

Foreman-Mackey, D., Agol, E., Ambikasaran, S., & Angus, R. 2017, *AJ*, 154, 220

Foreman-Mackey, D., Hogg, D. W., Lang, D., & Goodman, J. 2013, *PASP*, 125, 306

Fornasini, F., Antoniou, V., & Dubus, G. 2023, in *Handbook of X-ray and Gamma-ray Astrophysics*, 143

Foster, G. 1996, *AJ*, 112, 1709

Gross, E. & Vitells, O. 2010, *European Physical Journal C*, 70, 525

Haberl, F. 1991, *ApJ*, 376, 245

Hübner, M., Huppenkothen, D., Lasky, P. D., & Inglis, A. R. 2022a, *ApJS*, 259, 32

Hübner, M., Huppenkothen, D., Lasky, P. D., et al. 2022b, *ApJ*, 936, 17

Islam, N., Corbet, R. H. D., Coley, J. B., Pottschmidt, K., & Fürst, F. 2023, *ApJ*, 948, 45

Islam, N. & Paul, B. 2014, *MNRAS*, 441, 2539

Jin, C., Done, C., & Ward, M. 2020, *MNRAS*, 495, 3535

Kaper, L., van der Meer, A., & Najarro, F. 2006, *A&A*, 457, 595

Kelly, B. C., Becker, A. C., Sobolewska, M., Siemiginowska, A., & Uttley, P. 2014, *ApJ*, 788, 33

Koenigsberger, G., Georgiev, L., Moreno, E., et al. 2006, *A&A*, 458, 513

Koh, D. T., Bildsten, L., Chakrabarty, D., et al. 1997, *ApJ*, 479, 933

Kotze, M. M. & Charles, P. A. 2012, *MNRAS*, 420, 1575

Kreykenbohm, I., Wilms, J., Coburn, W., et al. 2004, *A&A*, 427, 975

Lien, A. Y., Krimm, H. A., Markwardt, C. B., et al. 2025, *ApJ*, 989, 161

Liu, J., Soria, R., Qiao, E., & Liu, J. 2018, *MNRAS*, 480, 4746

Lomb, N. R. 1976, *Ap&SS*, 39, 447

Manikantan, H., Kumar, M., Paul, B., & Rana, V. 2024, *MNRAS*, 527, 640

Martin, R. G. 2023, *MNRAS*, 523, L75

Moreno, E., Koenigsberger, G., & Toledano, O. 2005, *A&A*, 437, 641

Mundo, S. A. & Mushotzky, R. 2023, *MNRAS*, 526, 4040

Nabizadeh, A., Mönkkönen, J., Tsygankov, S. S., et al. 2019, *A&A*, 629, A101

Ogilvie, G. I. & Dubus, G. 2001, *MNRAS*, 320, 485

Pravdo, S. H., Day, C. S. R., Angelini, L., et al. 1995, *ApJ*, 454, 872

Pravdo, S. H. & Ghosh, P. 2001, *ApJ*, 554, 383

Ramiaramantsoa, T., Moffat, A. F. J., Harmon, R., et al. 2018, *MNRAS*, 473, 5532

Remillard, R. A. & McClintock, J. E. 2006, *ARA&A*, 44, 49

Romano, P., Cohen, H. I., Bozzo, E., et al. 2025, *A&A*, 699, A119

Sato, N., Nagase, F., Kawai, N., et al. 1986, *ApJ*, 304, 241

Scargle, J. D. 1982, *ApJ*, 263, 835

Sharma, A., Banerjee, A., Das, A. K., Mandal, A., & Bose, D. 2024, *ApJ*, 975, 56

Sood, R., Farrell, S., O'Neill, P., & Dieters, S. 2007, *Advances in Space Research*, 40, 1528

Stone, Z., Shen, Y., Burke, C. J., et al. 2022, *MNRAS*, 514, 164

Suleimanov, V. F., Forsslom, S. V., Tsygankov, S. S., et al. 2023, *A&A*, 678, A119

Tauris, T. M. & van den Heuvel, E. P. J. 2006, in *Compact stellar X-ray sources*, ed. W. H. G. Lewin & M. van der Klis, Vol. 39, 623–665

Timmer, J. & König, M. 1995, *A&A*, 300, 707

VanderPlas, J. T. 2018, *ApJS*, 236, 16

Vaughan, S., Uttley, P., Markowitz, A. G., et al. 2016, *MNRAS*, 461, 3145

White, N. E., Mason, K. O., Huckle, H. E., Charles, P. A., & Sanford, P. W. 1976, *ApJ*, 209, L119

White, N. E. & Swank, J. H. 1984, *ApJ*, 287, 856

Xu, J., Hu, S., Chen, X., & Huang, S. 2025, *ApJ*, 984, 45

Yang, S., Yan, D., Zhang, P., Dai, B., & Zhang, L. 2021, *ApJ*, 907, 105

Yu, W., Richards, G. T., Ruan, J. J., et al. 2025, *ApJ*, 992, 130

Yu, W., Richards, G. T., Vogeley, M. S., Moreno, J., & Graham, M. J. 2022, *ApJ*, 936, 132

Zalot, N., Sokolova-Lapa, E., Stierhof, J., et al. 2024, *A&A*, 686, A95

Zdziarski, A. A., Wen, L., & Gierliński, M. 2007, *MNRAS*, 377, 1006

Zhang, H., Yang, S., & Dai, B. 2023, *ApJ*, 946, 52

Zhang, P. 2024, *ApJ*, 972, 80

Zhu, X.-J. & Thrane, E. 2020, *ApJ*, 900, 117

Appendix A: Results of the GP Light Curve Modeling

In Fig. A.1, the upper panel presents the GP best-fit to the light curve, while the lower panel summarizes the residual diagnostics. The resulting standardized residuals are consistent with white noise: they pass the K–S test with $P = 0.28$, and the ACFs of both the SRs and the squared SRs lie within the 95% confidence bounds expected for a white-noise process.

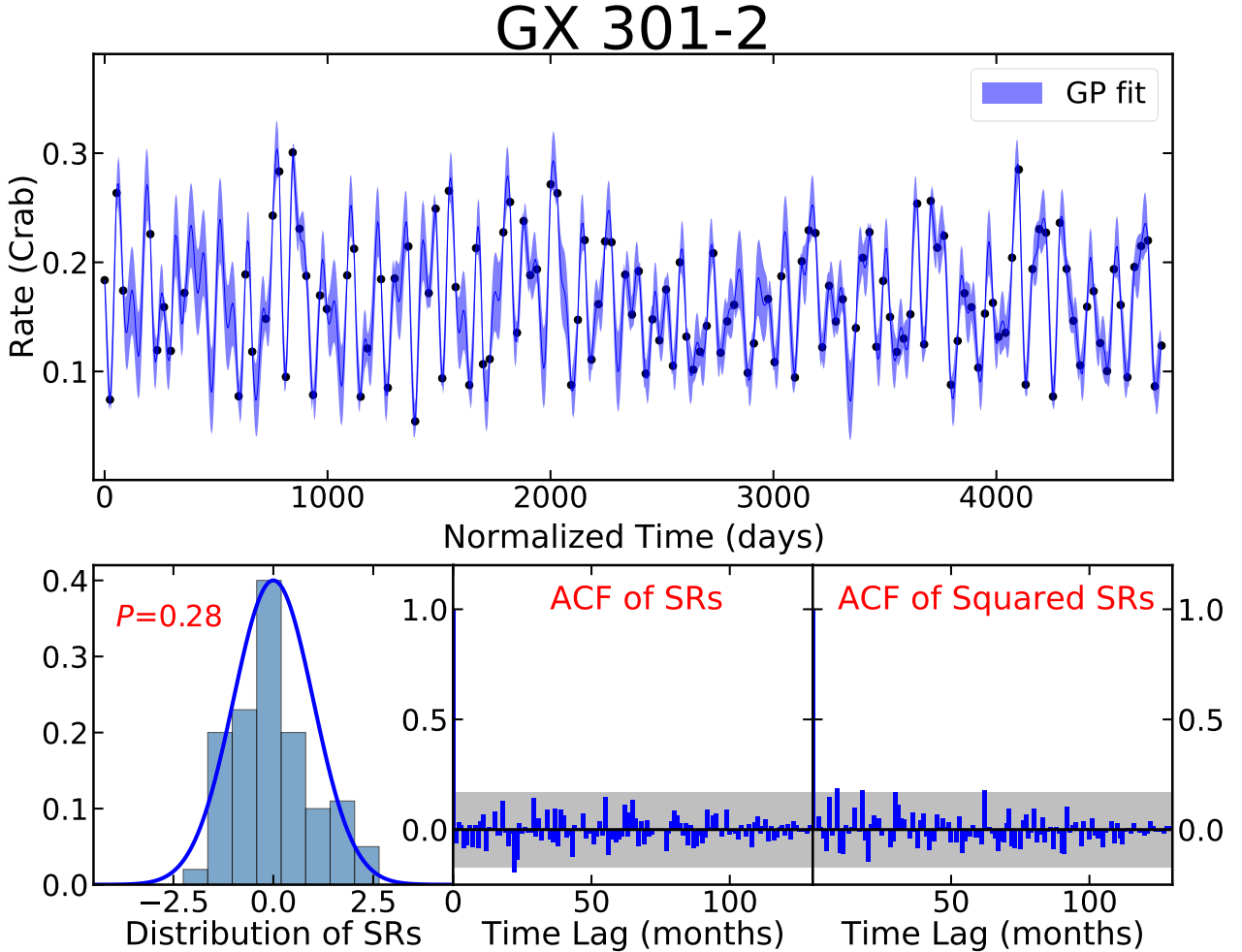


Fig. A.1. GP modeling of the long-term *Swift*/BAT 14–195 keV light curve of GX 301-2 and residual diagnostics. The top panel shows the observed light curve (black points) together with the GP reconstruction (blue band). The bottom-left panel shows the distribution of standardized residuals (SRs) with the K–S test P -value. The bottom-middle and bottom-right panels show the autocorrelation functions (ACFs) of the SRs and of the squared SRs, respectively; both are consistent with the expectations for a white noise process.

In Fig. A.2, we present the posterior distributions of the parameters inferred from the SHO + SHO model. All parameters show good convergence, further supporting the robustness of the modeling results.

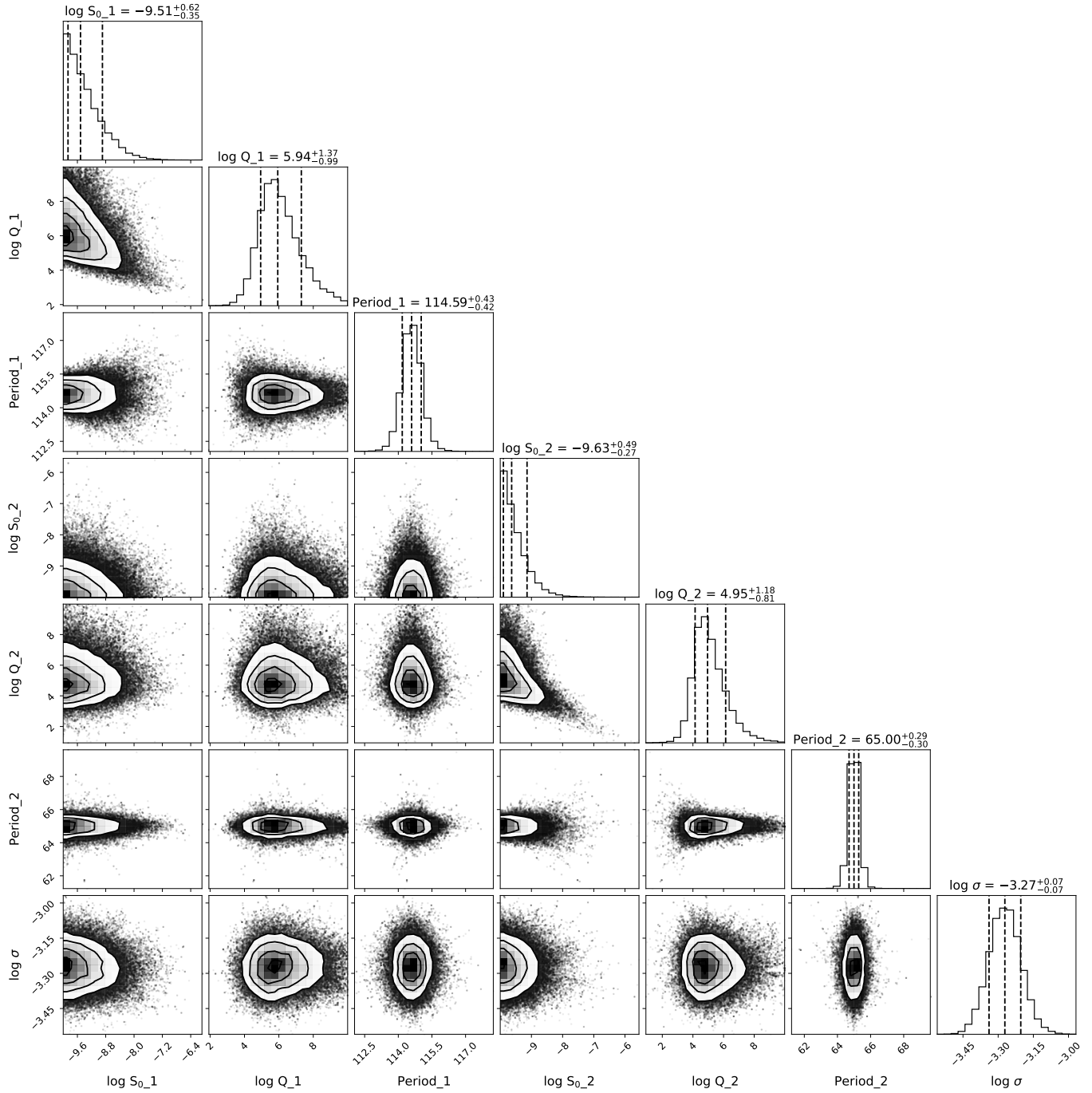


Fig. A.2. Posterior distributions of the GP model parameters inferred from the SHO + SHO fit to the *Swift*/BAT light curve of GX 301-2. The well-behaved posteriors indicate good convergence and support the robustness of the GP modeling.